



Dynamics of a partially wetting droplet under wind and gravity

Alireza Hooshanginejad *Department of Biological and Environmental Engineering, Cornell University, Ithaca, New York 14850, USA*Sungyon Lee **Department of Mechanical Engineering, University of Minnesota, Minneapolis, Minnesota 55455, USA*

(Received 10 September 2020; accepted 22 February 2022; published 4 March 2022)

Partially wetting drops are ubiquitous in nature and industry and are often subject to a combined forcing by wind and gravity. In particular, the stability of water drops under the combination of wind and other external forces is relevant in numerous applications that include aircraft de-icing, heat exchangers, and fuel cells. In this paper, we investigate the onset of droplet depinning from a solid substrate when a partially wetting water droplet is simultaneously exposed to high-Reynolds-number airflow and to gravity. We first develop simple scaling arguments which explain that the critical flow velocity for depinning, U_{cr} , and the droplet volume, V , scale as $U_{cr} \sim V^{-1/6}$ in the absence of gravitational effects, in good agreement with the existing experimental data. We then develop a two-dimensional model for a unidirectional flow over a slender drop under two scenarios: aligned with (downwind) or opposing the gravitational body force (upwind). Our results show a clear deviation in U_{cr} between the upwind and downwind cases as the droplet size is increased. The differences between these two regimes are further manifested in the distinct droplet shapes at the critical onset of depinning. Finally, we investigate the role of flow separation from the leeward side of the drop by systematically increasing the slope of the droplet surface at the separation point. Our results point to more pronounced effects of the flow separation in the upwind regime.

DOI: [10.1103/PhysRevFluids.7.033601](https://doi.org/10.1103/PhysRevFluids.7.033601)

I. INTRODUCTION

Water drops on the windshield of a moving vehicle are a familiar sight on any rainy day, and they are just one example of partially wetting droplets subject to wind and gravity forcing. Despite their ubiquity, predicting the threshold of droplet depinning under combined surface and body forces poses a problem of fundamental importance in fluid mechanics. From the practical standpoint, understanding the droplet stability under wind and gravity is relevant to numerous industrial processes, such as heat exchanger efficiency [1,2] and aircraft deicing [3,4]. When the imposed external flow falls in the high-Reynolds-number regime, the coupling of contact line dynamics and the unsteadiness associated with the inertial flow introduces significant complexity to the physical picture.

Due to this complexity, only limited studies have focused on the dynamics of partially wetting droplets that are driven by the high-Reynolds-number (Re) air flow [5–12]. The major challenge of high-Reynolds-number forcing is the coupled evolution of the droplet and the wind itself, which can lead to flow separation on the leeward side of the droplet at $Re \gtrsim 120$ [13]. Ding and Spelt [6,7] performed numerical simulations of droplet spreading under wind by including droplet inertia

*sungyon@umn.edu

into their calculations. However, they acknowledged that the effectiveness of their simulations was limited to $Re < 250$, due to the inherent unsteadiness of the separated flow in the contact line region. Circumventing the computational challenges in this flow regime, Durbin [5] developed a simplified lubrication model to study the stability threshold of partially wetting droplets on a horizontal surface under wind forcing. In this model, he imposed the separation of the external flow at different points along the droplet surface and assumed a constant pressure inside the separated flow, which we will also implement in our present study.

By contrast, the dynamics of partially wetting droplets subject to gravity have been extensively studied, both experimentally and theoretically [14–25]. Macdougall and Ockrent [14] found that the product of a droplet’s sideview area and the sine of the inclination angle at which the droplet first slides is independent of the droplet size. Later, Bikerman [15] investigated the changes in the contact line shape as a droplet evolves under gravity. Furmidge [16] studied the retention of spray droplets under gravity using a two-dimensional (2D) approach, in good agreement with the experiments. Building on the findings by Bikerman and Furmidge, Dussan [17,18] developed a lubrication model for droplet stability on inclined surfaces that empirically incorporate straight lines as segments of the contact line of the droplet. In a related work, Dimitrakopoulos and Higdon [23] performed three-dimensional computations to study the displacement threshold of partially wetting droplets on tilted surfaces due to the action of gravity.

More recently, White and Schmucker [26] investigated droplet stability on a roughened surface by uniquely combining the effects of inertial wind and gravity forcing. Specifically, they experimentally measured the critical wind speed at which a droplet dislodges from a tilted surface for varying droplet volumes. In particular, their experimental findings suggest new transitional behaviors in the threshold of depinning when wind and gravity are applied simultaneously. However, their work lacks a detailed theoretical model for the droplet shape that brings together the effects of the high-Re air flow and gravity.

In this paper, we construct a minimal 2D model of droplet depinning in the manner of Durbin [5], which implements the high-Re wind and the body force. In particular, we consider two distinct scenarios in which the applied wind force is aligned with or opposing the body force. The change in the direction of the applied wind relative to the body force has a nontrivial effect on the critical wind speed for depinning, as the force from the wind is directly coupled to the shape of the droplet. In addition, we investigate the effects of flow separation on the critical flow velocity by systematically varying the location of the separation point.

The paper is organized as follows: Section II comprises the scaling laws in the wind-only limit and validation against the experiments by White and Schmucker [26]. In Sec. III, we develop a 2D lubrication model that implements the effects of flow separation and gravity at the onset of droplet depinning. The results of the 2D model are presented in Sec. IV. Finally, we conclude with a summary and discussion of future work in Sec. V.

II. SCALING LAWS

A. Physical picture

Let us consider a partially wetting droplet under uniform air flow and gravity. In the absence of external forcing, a droplet assumes an axisymmetric shape with a diameter, l_0 , and an equilibrium contact angle, θ_0 , which is set by the wettability of the substrate. Then the application of wind or gravity deforms the droplet asymmetrically, so that the contact angle, $\theta(\beta)$, along the contact line deviates from θ_0 . The resultant asymmetry in $\theta(\beta)$ generates a net adhesive force, F_{adh} :

$$F_{\text{adh}} = -\sigma \oint \cos \theta(\beta) \hat{\mathbf{n}} \cdot \hat{\mathbf{i}} ds, \quad (1)$$

where ds is the differential element along the contact line [see Fig. 1(a)] and σ is the surface tension coefficient. Note that $\theta(\beta)$ may range from the minimum value, θ_r , to the maximum, θ_a ; $\Delta\theta = \theta_a - \theta_r$ is the contact angle hysteresis whose value is determined by the surface roughness and chemical

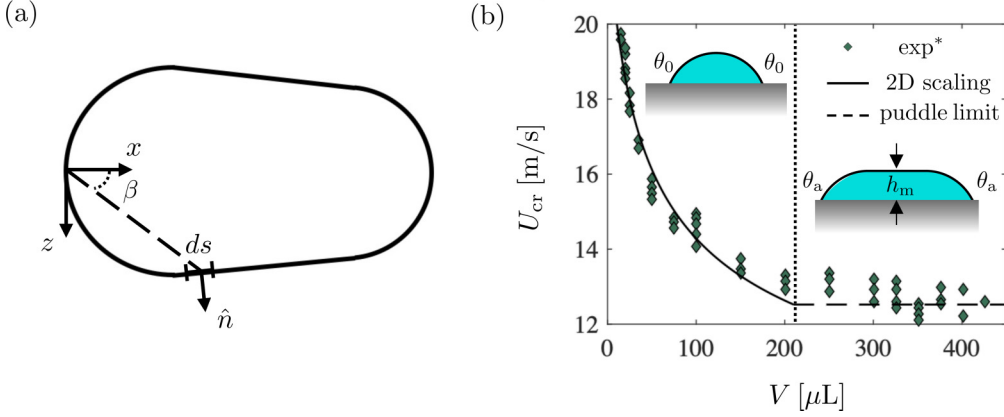


FIG. 1. (a) The top-view schematic of droplet's three-phase contact line. (b) The critical wind velocity, U_{cr} , for varying droplet volume, V on a horizontal surface (i.e., $\alpha = 0$). (Note that the experimental data are reproduced from Ref. [26].)

inhomogeneity of the given substrate. In particular, the adhesive force is at its maximum, or $F_{\text{adh}} \sim \sigma l_0 (\cos \theta_r - \cos \theta_a)$, when the advancing and receding contact angles reach θ_a and θ_r , respectively [14]. Only when the external forcing is large enough to overcome the maximum adhesive force does the droplet dislodge from the surface. Hereafter, we refer to this moment as the onset of *depinning*.

In this critical configuration, F_{adh} must be balanced by the combination of gravity, the pressure drag from the wind, F_w , and the viscous shear drag, F_s , arising from the boundary layer. The relative magnitudes of F_w and F_s depend on the Reynolds number associated with the external air flow or $\text{Re}_a = \rho_a U h_0 / \mu_a$. Here ρ_a and μ_a refer to the density and dynamic viscosity of air, respectively, and h_0 denotes the droplet's initial height. In the regime where $\text{Re}_a > 120$, the air flow separates around the droplet and causes a pressure drop in the wake region, so that $F_w \sim \rho_a l_0 h_0 U^2$ [13]. For simplicity, we use the initial height, h_0 , and width of the drop, l_0 , to approximate the relevant forces (e.g., F_w and F_{adh}), thereby neglecting the deformations of the droplet from its initial geometry. The dimensionless thickness of the boundary layer, δ/l_0 , scales as $\text{Re}_a^{-1/2} \varepsilon^{1/2}$, where $\varepsilon \equiv h_0/l_0$. Hence, the ratio between the pressure and shear forces corresponds to $(\text{Re}_a \varepsilon)^{1/2}$, as $F_s \sim (\mu_a U / \delta) l_0^2 \sim \mu_a U l_0 \text{Re}_a^{1/2} \varepsilon^{-1/2}$ [5, 11, 27].

B. Comparison with experiments

In the limit of $(\text{Re}_a \varepsilon)^{1/2} \gg 1$, we neglect the shear force, F_s , and balance F_{adh} and F_w in the absence of gravity, so that

$$\frac{C_D}{2} \rho_a U_{\text{cr}}^2 h_0 l_0 = C \sigma l_0 (\cos \theta_r - \cos \theta_a), \quad (2)$$

where C_D is the drag coefficient and C is an $O(1)$ geometric factor that accounts for integrating a contact angle profile, $\theta(\beta)$, around the contact line. The resultant scaling law for U_{cr} corresponds to $U_{\text{cr}} \sim 1/\sqrt{h_0}$ at the onset of depinning, which we hereby validate against the experimental data by White and Schmucker [26]. White and Schmucker [26] measured the critical wind speed, U_{cr} , at which a partially wetting water droplet of volume, V , dislodges from a roughened aluminum surface inside a miniature wind tunnel, with $\text{Re}_a \sim O(10^3)$. Their experiments reveal that the critical wind speed decreases with increasing droplet volume, V , until it reaches a plateau at ~ 12.5 m/s [see Fig. 1(b)].

Our scaling law suggests that this plateau in U_{cr} can be explained by examining how the initial droplet height, h_0 , varies with V . For small V , droplets assume a spherical cap geometry with an

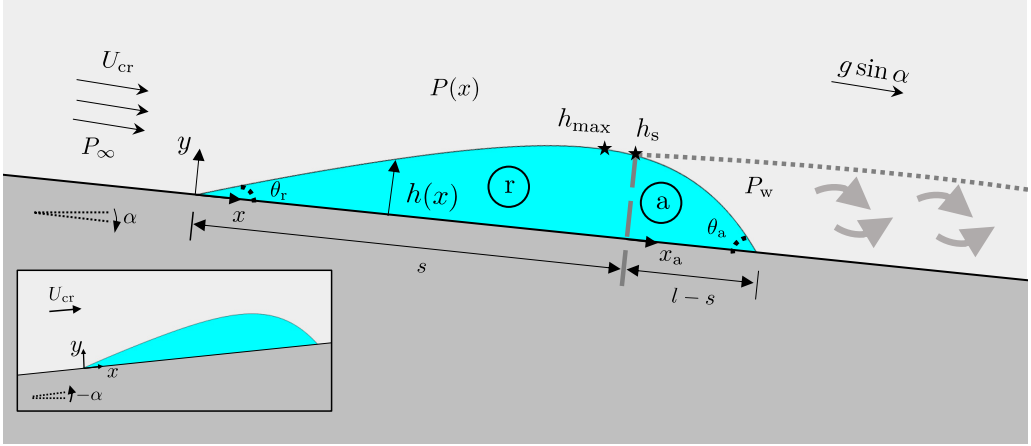


FIG. 2. The schematic of a 2D lubrication droplet on an inclined surface with an angle α , subject to uniform wind that is parallel to the substrate.

equilibrium contact angle, $\theta_0 = 49^\circ \pm 1^\circ$ [26], such that

$$h_0 = \left[\frac{6V \sin^2(\theta_0/2)}{\pi(2 + \cos \theta_0)} \right]^{1/3}, \quad (3)$$

which yields $U_{cr} \sim V^{-1/6}$. Figure 1(b) shows that the scaling relation $U_{cr} = 0.98V^{-1/6}$ is in good agreement with the experiments for $V \lesssim 200 \mu\text{l}$. The value of the prefactor (i.e., 0.98) implies that the value of the unknown parameters in Eq. (2), $\sqrt{C/C_D}$, is approximately equal to 2.7 or $C_D \sim O(0.1)$ if we assume $C \sim O(1)$.

For larger V , the droplet forms a puddle whose height is given by $h_m = 2\sqrt{\sigma/(\rho g)} \sin(\theta_a/2)$, [28] where ρ denotes water droplet density and $\theta_a = 63.5^\circ \pm 3.7^\circ$ [26]. Notably, we conjecture that h_m depends on θ_a , instead of $\theta_0 = 49^\circ \pm 1^\circ$, since the contact line most likely advances to form a puddle as the droplet volume is gradually added from a syringe. Therefore, for large droplets, the droplet's height becomes independent of V , which coincides with the plateau in U_{cr} as shown in Fig. 1(b). Then, this transitional droplet volume, V_c , can be determined by equating Eq. (3) to h_m , so that

$$V_c = \frac{4\pi}{3} (2 + \cos \theta_0) \left(\frac{\sigma}{\rho g} \right)^{3/2} \left[\frac{\sin^3(\theta_a/2)}{\sin^2(\theta_0/2)} \right]. \quad (4)$$

Based on the given experimental parameters, we obtain $V_c \approx 210 \mu\text{l}$, which is in good agreement with the experiments with no fitting parameters. In addition, if we replace h_0 with $h_m = 2\sqrt{\sigma/(\rho g)} \sin(\theta_a/2)$ in Eq. (2) and $\sqrt{C/C_D} \approx 2.7$, then the value of the critical velocity approximately equals to 12.9 m/s, which closely matches the experimental plateau in U_{cr} in the large-droplet limit. More importantly, the effectiveness of the scaling law demonstrates that it correctly captures the key physical features of the wind-only regime: pressure drag and adhesive force.

If we place the droplet on a tilted surface prior to applying a uniform wind, then the force balance at the onset of depinning becomes $F_{adh} \sim F_w + \rho g V \sin \alpha$, where α is the angle of surface inclination, as illustrated in Fig. 2. Interestingly, as demonstrated in Ref. [26], this simple force balance can no longer successfully rationalize the experimental measurements of U_{cr} that exhibit a V -dependent transition for $\alpha > 0^\circ$. One clear limitation of the scaling laws is that they do not account for the deviation of the droplet geometry from its initial axisymmetric state. While the use of h_0 and l_0 to approximate F_w may be reasonable for $\alpha = 0^\circ$, the neglect of droplet deformations

becomes problematic in the presence of the body force that further deforms the droplet. Hence, given the limited success of the scaling laws, we aim to compute the droplet shape at the onset of depinning to gain further understanding of the droplet dynamics under wind and gravity.

III. 2D MODEL

A. Model simplifications

Building on the scaling law in Sec. II, we develop a simplified 2D lubrication model that incorporates the barebones physical ingredients, namely the flow separation over the droplet under wind, gravity, and surface tension effects. Hence, we make a number of simplifying assumptions in our model, which we summarize here. Note that the goal of the 2D model is no longer to validate the existing experimental data but to gain general understanding of the effects of wind and gravity on droplet depinning.

First, we model the system as completely two-dimensional, neglecting variations in the z direction. The 2D model cannot quantitatively resolve the flow inside the three-dimensional droplet; however, the current model is able to capture some physical features of the droplet dynamics, including the droplet shape at the onset of depinning, due to the quasi-2D nature of the external flow. Second, we assume that the 2D droplet is “thin” (i.e., the aspect ratio, $\varepsilon \ll 1$), which allows us to employ lubrication approximations and reduce the governing equations. Third, consistent with Ref. [5], we take the limit of $(\text{Re}_a \varepsilon)^{1/2} \gg 1$ (or $\text{Re}_a \sim \varepsilon^{-3}$) and neglect the effects of viscous shear over the droplet in comparison to the pressure drag.

Furthermore, we assume the droplet is quasisteady prior to depinning. In the flow regime of $\text{Re}_a \sim \varepsilon^{-3}$, the droplet is expected to oscillate due to flow separation and vortex shedding. However, we assume that the timescale of droplet oscillations is much smaller than that of droplet evolution and depinning. This assumption is reasonable when the timescale associated with the increase in air flow is less than the characteristic capillary timescale (i.e., $t_{\text{capillary}} = \sqrt{\rho V / \sigma} \approx 0.02\text{--}0.15$ s), as is the case in Ref. [26]. Finally, we implement the separation of the external flow into our model with two notable simplifying approaches. First, we treat the location of the separation point to be a known input parameter, and we vary it systematically from the apex of the drop to further downstream. Second, aft of the separation point, we assume that the wake has a zero relative pressure, following the work of Ref. [5].

B. A two-dimensional lubrication model

As illustrated in Fig. 2, we consider a 2D water droplet of height, $h(x)$, that is at the onset of depinning on a surface with a tilting angle, α , subject to a uniform wind speed, U_{cr} . The small parameter, ε , corresponds to the ratio between the characteristic droplet height (e.g., h_{max}) and the droplet length, l . Note that α may range from negative to positive values, so that gravity may oppose (i.e., $\alpha < 0$) or be aligned with the imposed air flow (i.e., $\alpha > 0$). To define the criterion for depinning, we set θ_r and θ_a as the critical receding and advancing contact angles in our model, respectively. In addition, the external flow separates from the drop surface at a distance, s , from the receding contact line, and at a height, $h(x = s) = h_s$. Finally, we treat U_{cr} as an input parameter and compute the shape and, hence, the size of the droplet that depins at given U_{cr} . The advantage of using this “reverse” approach lies in the mathematical simplifications, which will become evident as we proceed. Furthermore, in the current model framework, the final length of the droplet, l , is not known *a priori* and comes out of the model calculation.

Under the quasistatic assumption, the force balance in the x direction over a differential control volume inside the drop yields

$$\rho g \sin \alpha - p'(x) = 0, \quad (5)$$

where $p(x)$ is the droplet's internal pressure and the prime denotes differentiation with respect to x . The droplet's internal pressure gradient comprises three physical effects:

$$p'(x) = P'(x) - \sigma h'''(x) + \rho g h'(x) \cos \alpha, \quad (6)$$

which are the gradient in the external pressure, the capillary pressure under lubrication approximation, and the hydrostatic pressure, respectively.

Specifically, the presence of the drop locally perturbs the external flow and leads to a nonuniform pressure, $P(x)$, over the drop, which eventually leads to the separation of the boundary layer. As δ/l scales as $\text{Re}_a^{-1/2} \varepsilon^{1/2}$ with $\text{Re}_a \sim \varepsilon^{-3}$, we assume that the boundary layer thickness, δ , is much thinner than the drop height (i.e., $\delta/h \ll 1$). Mass conservation of the external flow covering the drop prior to separation dictates that $U(x)(1 - h(x)/H) = U_{\text{cr}}$, where $U(x)$ is the average external wind velocity over the droplet. Here H is the characteristic length from the substrate where the perturbed flow transitions to a uniform flow. In this study, we use $H = 5$ cm for simplicity. Then, based on the Bernoulli equation, we obtain $P'(x) = -\rho_a U U'(x)$, which reduces to $P'(x) = -\rho_a U_{\text{cr}}^2 h'(x)/H$ in the limit of $h/H \ll 1$. We note that the results of our model remain qualitatively unchanged with different values of H as long as $h/H \ll 1$.

We now divide the droplet's configuration at the onset of depinning into two regions: the receding side that is attached to the external flow (denoted with "r") and the advancing side exposed to the wake (denoted with "a") in Fig. 2. Equation (5) on the receding side corresponds to

$$\sigma h_r'''(x) + (\rho_a U_{\text{cr}}^2/H - \rho g \cos \alpha) h_r'(x) + \rho g \sin \alpha = 0, \quad (7)$$

where h_r denotes the droplet's height in the receding region. Note that Eq. (7) is only valid for $x = [0, s]$. The boundary conditions for Eq. (7) are

$$h_r(x=0) = 0, \quad h_r'(x=0) = \tan \theta_r, \quad h_r'(x=s) = 0. \quad (8)$$

Note that the last condition corresponds to the assumption of flow separation at the apex of the droplet.

On the advancing side, we assume that the pressure in the wake is a constant, so that $P'(x) = 0$. Therefore, Eq. (5) in the advancing region yields

$$\sigma h_a'''(x) - \rho g \cos \alpha h_a'(x) + \rho g \sin \alpha = 0, \quad (9)$$

where h_a denotes the droplet's height in the advancing region. Note that the droplet on the advancing side is primarily governed by gravity and capillarity only. In addition, Eq. (9) is only valid for $x_a = [0, l - s]$, where $x_a = x - s$. The boundary conditions for Eq. (9) are given by

$$h_a(x_a = l - s) = 0, \quad h_a'(x_a = l - s) = -\tan \theta_a, \quad h_a'(x_a = 0) = 0. \quad (10)$$

With the current set of ODE's and boundary conditions, we can derive analytical solutions for the droplet profile on each side [i.e., $h_r(x)$ and $h_a(x_a)$] at given U_{cr} and α with l and s still unknown. Then, to find l and s , we consider the two matching conditions at the separation point:

$$h_r(s) = h_a(0), \quad h_r''(s) - h_a''(0) = \frac{1}{\sigma} [P(s) - P_w], \quad (11)$$

where P_w is the constant pressure in the wake. Specifically, the latter condition accounts for the pressure drag force exerted on the droplet. Note that we only retain the leading-order term of the external pressure upstream of the separation point and neglect the external pressure variations over the drop which scale as $O(\varepsilon)$, such that $P(s) \approx P_\infty$.

Finally, we close the problem and compute s and l by solving a system of two coupled nonlinear equations in Eq. (11). This results in the complete solutions for $h_r(x)$ and $h_a(x_a)$, which are integrated to yield the droplet area, A ,

$$A = \int_0^s h_r dx + \int_0^{l-s} h_a dx_a, \quad (12)$$

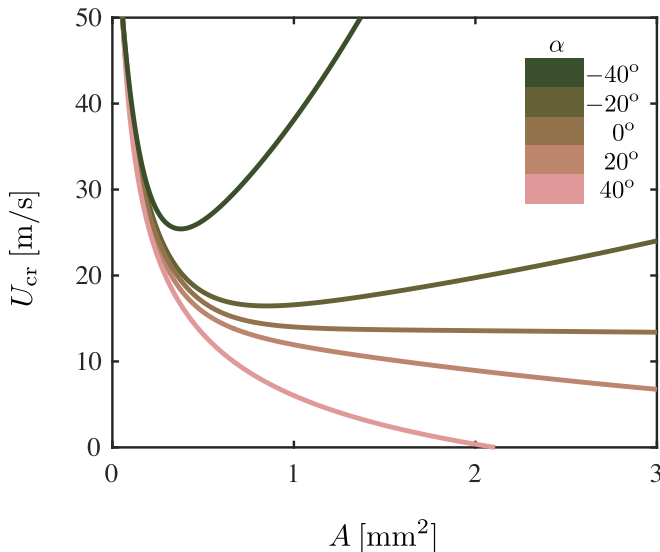


FIG. 3. The plot of U_{cr} versus A for $\alpha = 0^\circ, \pm 20^\circ$, and $\pm 40^\circ$.

for given U_{cr} and α . Note that taking the droplet size (i.e., area) as the input instead of U_{cr} significantly complicates the current procedure as we need further assumptions to find both U_{cr} and $h(x)$ that corresponds to the given droplet size.

Next, to explore the effects of flow separation on depinning conditions, we vary the slope of the droplet profile at which the flow separates. This requires rewriting the boundary conditions in Eq. (7) and Eq. (9) corresponding to the slope of the separation point as

$$h'_r(s) = -\tan \phi, \quad h'_a(0) = -\tan \phi, \quad (13)$$

where ϕ denotes the slope at the separation point. Then, for given U_{cr} , α , and ϕ , we can compute $h_r(x)$ and $h_a(x_a)$, as well as the droplet size, A , by following the same steps as previously described.

IV. MODEL RESULTS

A. Effects of gravity

In this section, we discuss the results from the 2D model introduced in Sec. III. For all cases presented here, we keep $\theta_r = 5^\circ$, $\theta_a = 30^\circ$, and $H = 5$ cm. We first modulate the effects of the body force parallel to the substrate by varying the values of the inclination angle, α , such that $\alpha = 0^\circ, \pm 20^\circ$, and $\pm 40^\circ$. Note that we currently set $\phi = 0$ and assume that the flow separates at the apex of the droplet.

Figure 3 shows the resultant plot of U_{cr} as a function of A for different values of α . In the limit of small A , U_{cr} rapidly decreases with A , independent of the sign and the value of α , as the effects of the body force are negligible. For larger A , U_{cr} exhibits two distinct behaviors depending on the value of α . For $\alpha \geq 0$, U_{cr} monotonically decreases with the droplet area with a slope that is proportional to the value of α . For instance, at $\alpha = 40^\circ$, U_{cr} reaches zero around $A \approx 2$ mm², which corresponds to the limit in which the body force alone is sufficient to depin the droplet. By contrast, at $\alpha = 0^\circ$, U_{cr} appears to gradually plateau to a constant value in the limit of large A . This result at $\alpha = 0^\circ$ qualitatively matches the experimental measurements of U_{cr} by White and Schmucker [26], which are reproduced in Fig. 1(b).

In the case of $\alpha < 0$, U_{cr} is no longer monotonically decreasing but starts to increase with A , as the body force directly opposes the applied wind and requires a higher wind speed to depin the

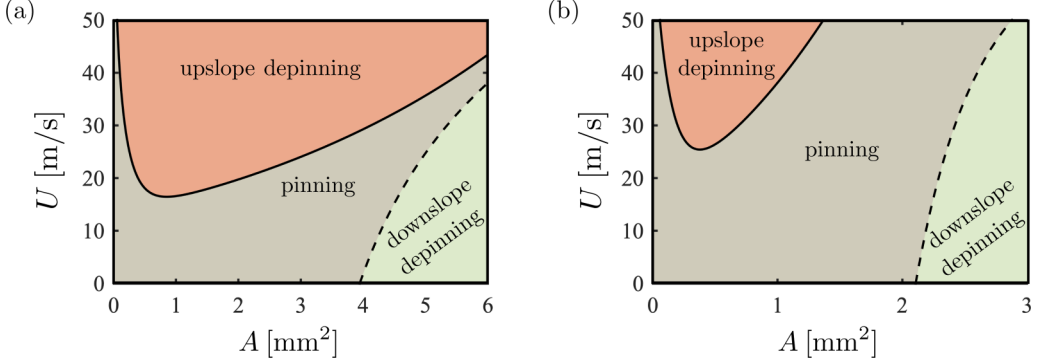


FIG. 4. The phase diagrams for droplet depinning behaviors (upslope depinning, pinning, and downslope depinning) for varying U and A at (a) $\alpha = -20^\circ$ and (b) for $\alpha = -40^\circ$.

given droplet. Furthermore, in this configuration, the drop can depin in either direction: upslope in the direction of the applied wind as shown in Fig. 3 or downslope in the direction opposing the wind. To find the downslope depinning criteria, we reverse the depinning boundary conditions in Eq. (10) and Eq. (13) and compute minimum A that satisfies the depinning condition for given U_{cr} and α . Figure 4 shows the phase diagrams summarizing three different droplet behaviors (upslope depinning due to wind, pinning, and downslope depinning due to gravity) at $\alpha = -20^\circ$ and $\alpha = -40^\circ$, respectively. As shown in Fig. 4, at low U , small droplets stay pinned as their weight is not sufficient to cause depinning, while large droplets depin downslope in the direction of gravity. As U reaches a threshold (i.e., $U \approx 17$ m/s for $\alpha = -20^\circ$, and $U \approx 25$ m/s for $\alpha = -40^\circ$) a new regime of upslope depinning emerges for a midrange size of drops. Notably, the region of upslope depinning spans a much wider range of droplet sizes for $\alpha = -20^\circ$ compared to $\alpha = -40^\circ$, as wind is more likely to overcome gravity for smaller negative α .

Focusing on the case of upslope depinning in Fig. 3, the droplet area at which U_{cr} starts to increase [i.e., $U'_{\text{cr}}(A) = 0$] is smaller for larger negative values of α . To rationalize this transitional behavior in U_{cr} , we revisit a simple 2D force balance on the droplet at the critical onset, namely:

$$\frac{C_D}{2} \rho_a U_{\text{cr}}^2 h_s + \rho g A \sin \alpha = \sigma (\cos \theta_r - \cos \theta_a). \quad (14)$$

Unlike the body force whose overall magnitude is fixed by the droplet size and α , the pressure drag requires integrating the pressure distribution around the droplet, which inherently depends on the droplet shape and, in particular, on h_s . Hence, we have replaced h_0 in Sec. II B with h_s , as it is a more accurate scale for the projected area over which the wind pressure acts. If we assume that $h_s = h_s(\alpha, A)$, then we can differentiate Eq. (14) with respect to A and obtain

$$\rho_a C_D U_{\text{cr}} \frac{\partial U_{\text{cr}}}{\partial A} h_s = \rho g \sin \alpha \left[\frac{\partial h_s}{\partial A} \left(\frac{A}{h_s} \right) - 1 \right] - \sigma (\cos \theta_r - \cos \theta_a) \frac{\partial h_s}{\partial A} \frac{1}{h_s}. \quad (15)$$

Equation (15) demonstrates that the sign of $U'_{\text{cr}}(A)$ is directly tied to how h_s varies with A .

Hence, we compute h_s from the lubrication model and plot it in Fig. 5(a), which shows a monotonic increase with A in an α -dependent manner. Specifically, h_s systematically increases as α is varied from $\alpha > 0$ to $\alpha < 0$. Due to the coupling of h_s with U_{cr} and gravity, h_s does not follow a simple power law of $A^{1/2}$ for small A ; instead, $h_s \propto A^{0.97}$ for $A < 0.1$ mm². As we can reasonably neglect the effects of gravity in this small- A limit, this steeper rise in h_s with A must be attributed to the combined effects of larger droplet volumes (or areas in the 2D model) and of the applied wind that tends to deform the droplet asymmetrically. The full behavior of h_s with A can be captured quantitatively in a cubic function that empirically relates $\ln h_s$ and $\ln A$, with one constant whose value depends on α . Based on this empirical function of h_s , we compute the transitional area A_c at

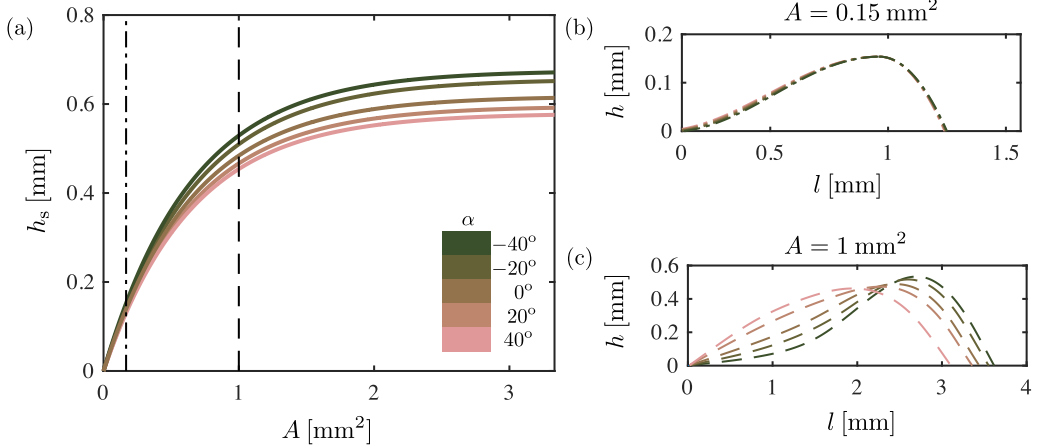


FIG. 5. (a) The plot of h_s as a function of A for $\alpha = 0^\circ, \pm 20^\circ, \pm 40^\circ$. The droplet profile, $h(x)$, at the onset of depinning for $\alpha = 0^\circ, \pm 20^\circ, \pm 40^\circ$ when (b) $A = 0.15 \text{ mm}^2$ and (c) $A = 1 \text{ mm}^2$.

which U_{cr} starts to increase, by setting $U'_{\text{cr}}(A) = 0$ in Eq. (15). The resultant values of A_c correspond to 1.0 mm^2 and 1.3 mm^2 for $\alpha = -40^\circ$ and $\alpha = -20^\circ$, respectively, which are slightly higher than what is observed in Fig. 3. This deviation likely stems from the neglect of the viscous shear force due to the lubrication flow inside the droplet in Eq. (14).

While the general increase in h_s is expected as the droplet size grows, the dependence of h_s on α has two compounding effects that cannot be easily decoupled. First, at A greater than 0.25 mm^2 , the value of U_{cr} is larger for more negative α . Hence, the rise in h_s for $\alpha < 0$ may be simply due to the increased wind speed that tends to deform the droplet more. At the same time, the orientation of the body force may itself influence the droplet shape in such a way that h_s increases when the body force opposes the incoming wind. However, the extent of the direct influence of α on the droplet shape remains unclear. Overall, the increase in h_s for $\alpha < 0$ must have some mitigating effects on the value of U_{cr} required to depin the given droplet.

In addition, Fig. 5(b) and Fig. 5(c) show $h(x)$ across all α at two distinct values of A : $A = 0.15 \text{ mm}^2$ and $A = 1 \text{ mm}^2$, respectively. At $A = 0.15 \text{ mm}^2$, there are hardly discernible differences in the droplet shapes across all α , which is consistent with the physical picture that the wind force dominates the body force at this value of A . Then, as A is increased (i.e., $A = 1 \text{ mm}^2$), the body force becomes more important, and the critical droplet shapes become strongly dependent on the value of α . In particular, at $A = 1 \text{ mm}^2$, the droplet is distinctly more elongated in the x direction with an increased maximum height, as α is systematically decreased from $+40^\circ$ to -40° . In addition, the curvature of the windward side of the drop changes from positive for $\alpha > 0$ to negative for $\alpha \leq 0$. The curvature change stems from the increasing external pressure in the windward side of the drop for decreasing α , consistent with a larger U_{cr} in this regime (see Fig. 3). Droplet profiles from the model are qualitatively compared with the experiments by White and Schmucker [26] for $\alpha \geq 0$ cases in the Appendix.

The growing differences in $h(x)$ as α is varied from $+40^\circ$ to -40° can be further quantified by measuring s/l , the x location of the droplet apex relative to its total length. As shown in Fig. 6, s/l increases with A for $\alpha \leq 0$. This implies that more fluid is shifted in the windward direction when the body force is either opposing or is not applied against the wind force. By contrast, s/l gradually decreases with increasing droplet size for $\alpha > 0$, suggesting that less fluid is shifted downstream when both the body force and the wind force act in the x direction. This slightly counterintuitive result points to the fact that the droplet shape is most strongly influenced by the value of U_{cr} than

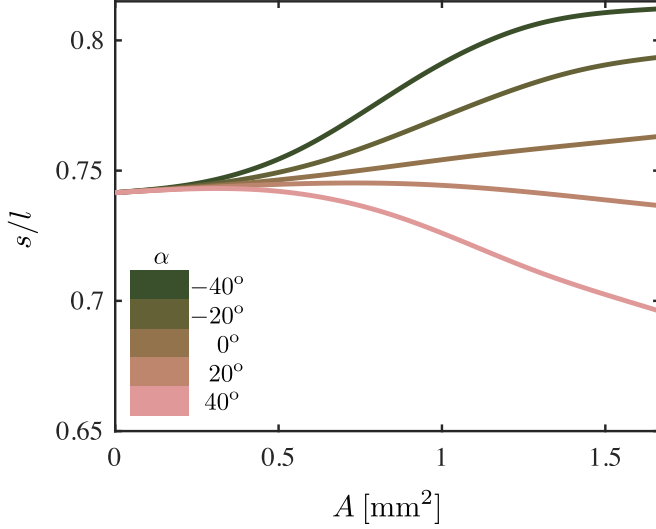


FIG. 6. The plot of s/l versus A for $\alpha = 0^\circ, \pm 20^\circ, \pm 40^\circ$ when $\phi = 0^\circ$.

the body force. In other words, larger U_{cr} leads to systematically larger s/l , and α must impact s/l via the resultant changes in U_{cr} .

B. Effects of flow separation

We explore how the flow separation may affect droplet depinning by systematically changing the slope, ϕ , of the line tangent to the droplet surface at the separation point [see schematics in Fig. 7(a) and Fig. 8(a)]. Due to the slender shape of the drop, we choose two additional cases of $\phi = 15^\circ$, and $\phi = 20^\circ$ in the leeward side of the drop, such that $\phi < \theta_a$. We focus on the effects of ϕ at two representative values of α , namely $\alpha = \pm 40^\circ$. As shown in Fig. 7(b), the increase in ϕ results in a clear decrease in h_s at $A = 1 \text{ mm}^2$, when α is set at -40° . Note that the separation point is marked

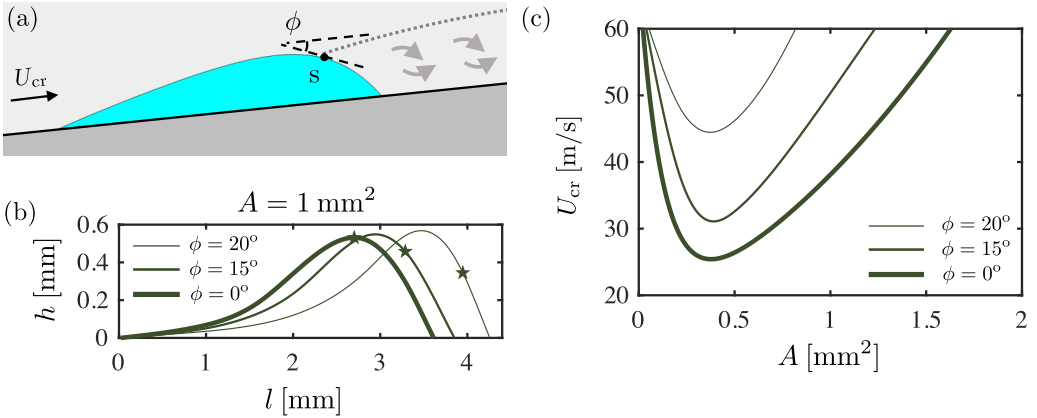


FIG. 7. (a) The schematic of flow separation in the upwind regime for $\alpha = -40^\circ$: ϕ is the slope of the line tangent to the droplet surface at the separation point. (b) The droplet profile for $\phi = 0^\circ, 15^\circ$, and 20° , while $A = 1 \text{ mm}^2$. The star symbol denotes the location of the separation point on the droplet surface. (c) The plot of U_{cr} versus A for $\phi = 0^\circ, 15^\circ$, and 20° .

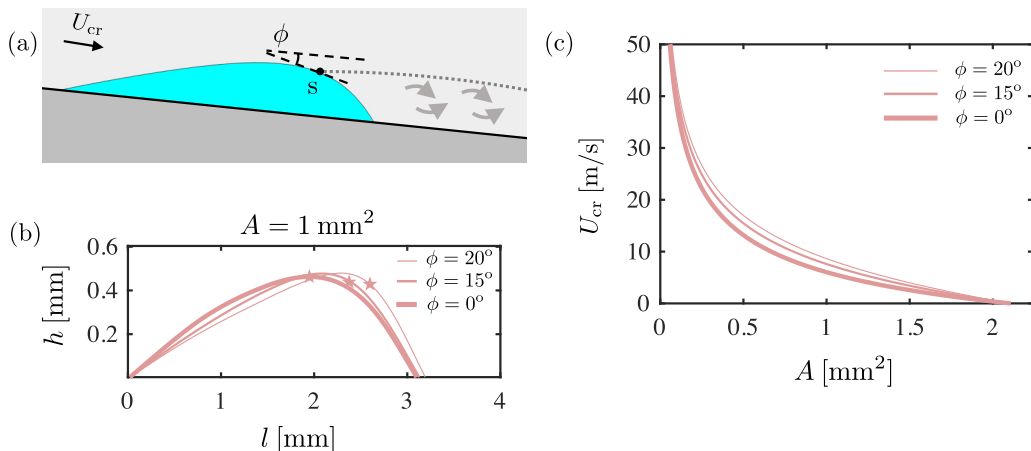


FIG. 8. (a) The schematic of flow separation in the upwind regime for $\alpha = 40^\circ$. (b) The droplet profile for $\phi = 0^\circ, 15^\circ$, and 20° , while $A = 1 \text{ mm}^2$. (c) The plot of U_{cr} versus A for $\phi = 0^\circ, 15^\circ$, and 20° .

with a star symbol on the droplet profiles in Fig. 7(b). Then, as plotted in Fig. 7(c), this reduction in h_s leads to a corresponding increase in U_{cr} with ϕ , as the total drag force required to depin the given droplet (i.e., $F_w \propto \rho_a U_{cr}^2 h_s$) remains unchanged.

By contrast, the effects of ϕ on droplet depinning are relatively minimal when $\alpha = 40^\circ$. As shown in Fig. 8(b), the increase in ϕ only slightly decreases h_s at $A = 1 \text{ mm}^2$, which leads to corresponding slight deviations in U_{cr} . Such reduced changes in h_s are due to the fact that the droplet shape near and downstream of the apex is less steep at $\alpha = 40^\circ$ compared to $\alpha = -40^\circ$, as clearly illustrated in Fig. 5(c). Furthermore, as shown in Fig. 8(c), ϕ -dependent changes in U_{cr} appear to vanish in the limit of both small and large A at $\alpha = 40^\circ$, distinct from the case of $\alpha = -40^\circ$. Negligible differences in U_{cr} are expected at small A , since U_{cr} is so large overall that deviations in h_s do not cause notable variations in U_{cr} . Then, in the limit of large A , the deviations in U_{cr} once again vanish, as the body force alone acts to depin the droplet, and the flow separation becomes irrelevant. Overall, the position of the flow separation plays a more important role in droplet depinning when the body force is applied in the upwind direction.

V. SUMMARY AND DISCUSSION

In this paper, we theoretically study the depinning threshold of partially wetting droplets under the combined effects of gravity and high Reynolds airflow. We first construct a scaling argument rationalizing the experimental findings by White and Schmucker [26], who measured the critical wind speed, U_{cr} , required to dislodge a partially wetting water droplet from a roughened aluminum substrate inside a miniature wind tunnel. Their results showed that for $\alpha = 0^\circ$, U_{cr} plateaus to a constant value for droplets larger than $V > 200 \mu\text{l}$ that form a “puddle” with a constant height h_0 . We successfully rationalize this wind-only behavior by balancing the pressure drag that scales as $U_{cr}^2 h_0 l_0$ with the adhesive force that scales as l_0 , so that $U_{cr} \propto h_0^{-1/2}$. We then correctly predict the transitional droplet volume at which U_{cr} plateaus with no fitting parameters by considering how h_0 varies with the droplet volume, V .

In addition to the scaling laws, we develop a 2D lubrication model that incorporates the pressure drag associated with flow separation, as well as the effects of gravity and surface tension. Specifically, at given U_{cr} and the inclination angle, α , we compute the droplet profile at the onset of depinning in both upwind and downwind scenarios. In the downwind case ($\alpha > 0$), U_{cr} continuously decreases with increasing droplet size. On the other hand, in the upwind case ($\alpha < 0$), U_{cr} first decreases for small droplets for upslope depinning but starts to increase with the droplet size. Then,

beyond some critical droplet size that depends on the value of α , large droplets no longer depin with wind but always depin downslope in the direction of gravity. In addition, the droplet profile at the onset of depinning shows a highly α -dependent behavior, as the upwind regime yields more elongated drops with a higher degree of asymmetry. As the effective wind forcing is dependent on the droplet shape, our results suggest a potential coupling between the gravity and wind forcing modalities.

The upwind results explain a common observation of rain drops on the windshield of a moving vehicle where some drops move upslope, while others move downslope. It is noteworthy that vehicle wind shields are often designed with angles between -30° to -50° for aerodynamic drag considerations [29]. Based on our findings, for a given speed of the vehicle, there is a midrange size of drops that depin upslope. In addition, larger drops will depin downslope under gravity, while smaller drops remain pinned. Finally, we investigate the flow separation condition by systematically varying the slope of droplet surface (ϕ) at the separation point. Our model results show that U_{cr} increases as the separation slope increases in both the downwind and upwind regimes; however, the effects of ϕ are much more prominent in the upwind case.

While our 2D model is successful in uncovering the combined effects of wind and gravity on droplet depinning, it ultimately has its limitations as addressed earlier in Sec. III B. These limitations ensure that our model cannot fully describe all the different regimes of droplet depinning, observed experimentally by White and Schmucker [26]. Hence, as future research, we will follow the work of Ref. [30] and develop a three-dimensional lubrication model using a precursor film and disjoining pressure [30–36]. Finally, a coupled system of the drop internal flow, the boundary layer flow over the drop, and the outer potential flow needs to be considered for a more rigorous characterization of the separation point. For instance, the free streamline theory can be incorporated to find the exact position of flow separation under the high Reynolds number flow [5,37,38]. A more rigorous model will be needed to find optimal strategies to effectively dry and clean partially wet surfaces.

ACKNOWLEDGMENTS

We thank Prof. E. White (TAMU) for fruitful discussions and experimental data. This work is supported by the National Science Foundation (Grant No. CBET-1605947).

APPENDIX: COMPARISON OF DROPLET PROFILES WITH EXPERIMENTS

We presently revisit the existing experimental data by White and Schmucker [26] who applied gravity and uniform air flow on partially wetting water droplets in a downwind configuration. They experimentally extracted the critical air velocity, U_{cr} , at which a given water droplet with volume, V , depins from a tilted aluminum substrate with $\theta_a = 63.5^\circ \pm 3.7^\circ$ and $\theta_r = 8.2^\circ \pm 1.5^\circ$. In all their experiments, the component of gravity parallel to the substrate is aligned with the incoming air flow (e.g., $\alpha = 0^\circ, 10^\circ, 20^\circ$, and 30°). Furthermore, the characteristic value of Re_a in Ref. [26] corresponds to $O(10^3)$ in the regime where the wind forcing dominates gravity.

Figure 9 comprises the side-view profiles of the droplets at the onset of depinning for both experiments and theory. Notably, the experimental results by White and Schmucker [26] at given α reveal that the critical droplet profiles collapse into a single profile for all values of U_{cr} when scaled by the length of the droplet. The shaded region in the experimental droplet profiles are indicative of some spread in the droplet shapes across all droplet sizes. Experimentally, there are slight differences between the side-view profiles in what they call the wind-dominated regime (i.e., $U_{cr} > 11$ m/s) that are shown in solid lines and the gravity-dominated regime (i.e., $U_{cr} < 11$ m/s) in dashed lines [26].

The theoretically computed droplet profiles in Fig. 9(b) show a similar collapse for the range of U_{cr} considered, when also normalized by the total droplet length, l . The results are computed for

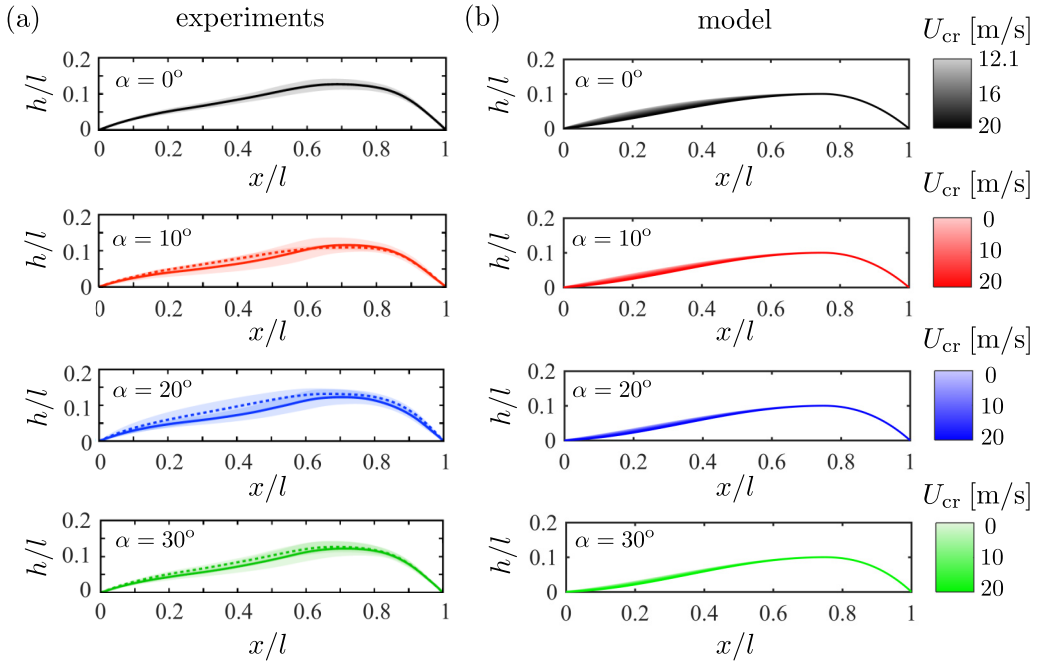


FIG. 9. (a) Droplet shapes in the experiments normalized by the final length, l , for different values of α . The shaded area indicates the span of droplet profile in the parametric experiments. (b) The droplet shape from the model results normalized by l for varying U_{cr} at different α . The colormap indicates the variations in U_{cr} .

$\theta_r = 5^\circ$, $\theta_a = 30^\circ$, and $\phi = 0$. Note that this comparison between experiments and theory is merely *qualitative*, designed to highlight the self-similar nature of the critical droplet shapes.

-
- [1] S. G. Kandlikar and M. E. Steinke, Contact angles and interface behavior during rapid evaporation of liquid on a heated surface, *Int. J. Heat Mass Transf.* **45**, 3771 (2002).
 - [2] D. J. Preston, D. L. Mafra, N. Miljkovic, J. Kong, and E. N. Wang, Scalable graphene coatings for enhanced condensation heat transfer, *Nano Lett.* **15**, 2902 (2015).
 - [3] T. Cebeci and F. Kafyeke, Aircraft icing, *Annu. Rev. Fluid Mech.* **35**, 11 (2003).
 - [4] R. J. Kind, M. G. Potapczuk, A. Feo, C. Golia, and A. D. Shah, Experimental and computational simulation of in-flight icing phenomena, *Prog. Aeronaut. Sci.* **34**, 257 (1998).
 - [5] P. A. Durbin, On the wind force needed to dislodge a drop adhered to a surface, *J. Fluid Mech.* **196**, 205 (1988).
 - [6] H. Ding and P. Spelt, Inertial effects in droplet spreading: A comparison between diffuse-interface and level-set simulations. *J. Fluid Mech.* **576**, 287 (2007).
 - [7] H. Ding and P. D. M. Spelt, Onset of motion of a three-dimensional droplet on a wall in shear flow at moderate reynolds numbers, *J. Fluid Mech.* **599**, 341 (2008).
 - [8] J. A. Schmucker, H. C. Osterhout, and E. B. White, Speckle technique for dynamic drop profile measurement on rough surfaces, *Exp. Fluids* **52**, 123 (2012).
 - [9] J. A. Schmucker, Experimental investigation of wind-forced drop stability, Ph.D. dissertation, Texas A&M University, Department of Aerospace Engineering, 2013.
 - [10] A. Hooshanginejad and S. Lee, Droplet depinning in a wake, *Phys. Rev. Fluids* **2**, 031601(R) (2017).
 - [11] A. Hooshanginejad, C. Dutcher, M. J. Shelley, and S. Lee, Droplet breakup in a stagnation-point flow, *J. Fluid Mech.* **901**, A19 (2020).

- [12] F. Yeganehdoust, A. Amer, N. Sharifi, I. Karimfazli, and A. Dolatabadi, Droplet mobility on slippery lubricant impregnated and superhydrophobic surfaces under the effect of air shear flow, *Langmuir* **37**, 6278 (2021).
- [13] M. Acarlar and C. Smith, A study of hairpin vortices in a laminary boundary layer. Part 1. Hairpin vortices generated by a hemisphere protuberance, *J. Fluid Mech.* **175**, 1 (1987).
- [14] G. Macdougall and C. Ockrent, Surface energy relations in liquid/solid systems. i. The adhesion of liquids to solids and a new method of determining the surface tension of liquids. *Proc. R. Soc. Lond. A* **180**, 151 (1942).
- [15] J. J. Bikerman, Sliding drops from surface of different roughness, *J. Colloid Sci.* **5**, 349 (1950).
- [16] C. G. L. Furmidge, Studies at phase interfaces. I. The sliding of liquid drops on solid surfaces and a theory for spray retention, *J. Colloid Sci.* **17**, 309 (1962).
- [17] E. B. Dussan V. and R. T.-P. Chow, On the ability of drops or bubbles to stick to non-horizontal surfaces of solids, *J. Fluid Mech.* **137**, 1 (1983).
- [18] E. B. Dussan V., On the ability of drops or bubbles to stick to non-horizontal surfaces of solids. Part 2. Small drops or bubbles having contact angles of arbitrary size, *J. Fluid Mech.* **151**, 1 (1985).
- [19] D. Quéré, M. Azzopardi, and L. Delattre, Drops at rest on a tilted plane, *Langmuir* **14**, 2213 (1998).
- [20] C. W. Extrand and Y. Kumagai, Liquid drops on an inclined plane: The relation between contact angles, drop shape, and retentive force, *J. Colloid Interface Sci.* **170**, 515 (1995).
- [21] H.-Y. Kim, H. J. Lee, and B. H. Kang, Sliding of liquid drops down an inclined solid surface, *J. Colloid Interface Sci.* **247**, 372 (2002).
- [22] C. Lv, C. Yang, P. Hao, F. He, and Q. Zheng, Sliding of water droplets on microstructured hydrophobic surfaces, *Langmuir* **26**, 8704 (2010).
- [23] P. Dimitrakopoulos and J. J. L. Higdon, On the gravitational displacement of three-dimensional fluid droplets from inclined solid surfaces, *J. Fluid Mech.* **395**, 181 (1999).
- [24] A. I. ElSherbini and A. M. Jacobi, Liquid drops on vertical and inclined surfaces: I. An experimental study of drop geometry, *J. Colloid Interface Sci.* **273**, 556 (2004).
- [25] A. I. ElSherbini and A. M. Jacobi, Liquid drops on vertical and inclined surfaces: II. A method for approximating drop shapes, *J. Colloid Interface Sci.* **273**, 566 (2004).
- [26] E. B. White and J. A. Schmucker, Wind- and gravity-forced drop depinning, *Phys. Rev. Fluids* **6**, 023601 (2021).
- [27] F. T. Smith, P. W. M. Brighton, P. S. Jackson, and J. C. R. Hunt, On boundary-layer flow past two-dimensional obstacles, *J. Fluid Mech.* **113**, 123 (1981).
- [28] P. G. de Gennes, F. Brochard-Wyart, and D. Quéré, *Capillarity and Wetting Phenomena* (Springer, Berlin, 2004).
- [29] V. S., V. S. Gangad, J. V., Maheswarreddy, A. Krishna, and Y. S Mukkamala, Windscreen angle and hood inclination optimization for drag reduction in cars, *Proc. Manufact.* **30**, 685 (2019).
- [30] L. Espín and S. Kumar, Droplet wetting transitions on inclined substrates in the presence of external shear and substrate permeability, *Phys. Rev. Fluids* **2**, 014004 (2017).
- [31] L. Espín and S. Kumar, Droplet spreading and absorption on rough, permeable substrates, *J. Fluid Mech.* **784**, 465 (2015).
- [32] J. Park and S. Kumar, Droplet sliding on an inclined substrate with a topographical defect, *Langmuir* **33**, 7352 (2017).
- [33] T. Pham and S. Kumar, Drying of droplets of colloidal suspensions on rough substrates, *Langmuir* **33**, 10061 (2017).
- [34] N. Savva and S. Kalliadasis, Dynamics of moving contact lines: A comparison between slip and precursor film models, *Europhys. Lett.* **94**, 64004 (2011).
- [35] L. W. Schwartz and R. R. Eley, Simulation of droplet motion on low-energy and heterogeneous surfaces, *J. Colloid Interface Sci.* **202**, 173 (1998).

- [36] L. W. Schwartz, Hysteretic effects in droplet motions on heterogeneous substrates: Direct numerical simulation, [Langmuir](#) **14**, 3440 (1998).
- [37] M. N. J. Moore, L. Ristroph, S. Childress, J. Zhang, and M. J. Shelley, Self-similar evolution of a body eroding in a fluid flow, [Phys. Fluids](#) **25**, 116602 (2013).
- [38] L. Ganedi, A. U. Oza, M. Shelley, and L. Ristroph, Equilibrium Shapes and their Stability for Liquid Films in Fast Flows, [Phys. Rev. Lett.](#) **121**, 094501 (2018).